Research Square

Preprints are preliminary reports that have not undergone peer review.
They should not be considered conclusive, used to inform clinical practice,
or referenced by the media as validated information.

Integrated Multiscale Pore-Network Characterization and Waterflood Modeling of Mixed-Wet Tight Sandstone Reservoirs

Yue Shi
China University of Geosciences (Beijing)
Bo Zhang
Research Institute of Petroleum Exploration and Development
Zhaohui Zhou
zhouzhaohui@petrochina.com.cn

Research Institute of Petroleum Exploration and Development
Yanfei Wang
Qinghai Meteorological Bureau

Research Article

Keywords: tight sandstone reservoir, pore structure, imbibition transient analysis, pore network modeling

Posted Date: November 20th, 2026

DOI: https://doi.org/10.21203/rs.3.rs-11588669/v1

License: This work is licensed under a Creative Commons Attribution 4.0 International License.
Read Full License

Additional Declarations: No competing interests reported.

Integrated Multiscale Pore-Network Characterization and Waterflood Modeling of Mixed-Wet Tight Sandstone Reservoirs

Yue Shi[1], Bo Zhang[2], Zhaohui Zhou[2*], Yanfei Wang[3,4*]

[1] *China University of Geosciences (Beijing), Beijing, 100083, China*

[2]*State Key Laboratory of Enhanced Oil & Gas Recovery, PetroChina Research Institute of Petroleum Exploration & Development, Beijing, 100083, China*

[3] *Qinghai Energy Bureau, Xining, 810008, China*

[4] *CNOOC China Limited, Shenzhen Branch, 518054, China*

* Corresponding author

E-mail address: zhouzhaohui@petrochina.com.cn (Z. Zhou), Wangyf@cnooc.com.cn (Y. Wang)

Abstract

Tight sandstone reservoirs often show early water breakthrough and low secondary recovery because injected water preferentially flows through a small fraction of connected pathways while bypass poorly connected and oil-wet pore domains where residual oil remains trapped. However, conventional pore-size characterization alone cannot determine which pore domains are accessible to water or oil, nor can it predict how wettability heterogeneity controls waterflood displacement. In this study, we develop a workflow that integrates multiscale pore-structure characterization, wettability-resolved pore-size analysis, together with mixed-wet pore-network modeling to diagnose the pore-scale controls on waterflood performance in a tight sandstone reservoir. In this workflow, MICP and N_2 adsorption were used to characterize pore-throat sizes from micrometer-scale throats to nanoscale pores, whereas nano-CT and centrifuge-NMR were used to evaluate pore connectivity and oil mobility. Comparative oil and brine imbibition data were interpreted using imbibition transient analysis (ITA) to obtain wettability-resolved pore size distributions. The experimentally obtained pore structure properties and wettability characteristics were then incorporated into an OpenPNM-based mixed-wet pore-network model. The results suggest that chemical EOR strategies for this reservoir should not rely solely on ultralow IFT. Instead, formulations capable of accessing and altering oil-wet nanoscale pore domains are more likely to improve microscopic sweep efficiency and mobilize residual oil.

Keywords: tight sandstone reservoir, pore structure, imbibition transient analysis, pore network modeling

Introduction

Tight sandstone reservoirs have become increasingly important hydrocarbon targets as global energy demand remains high and conventional resources mature (IEA, 2023; U.S. EIA, 2013). In China, continental shale oil and tight oil are important unconventional resources, and play significant role in the oil and gas supply. However, their economic development is commonly limited by small pore throats, strong heterogeneity, and poor natural connectivity (Zhao et al., 2020; Lai et al., 2018). During waterflooding, the complex and heterogeneous pore-throat system often results in reduced injectivity, uneven sweep, early water breakthrough, rapidly increasing water cut, and substantial residual oil retention (Yang et al., 2022; Liu et al., 2023). Therefore, improving recovery from tight sandstone reservoirs requires a pore-scale understanding of how pore structure and wettability jointly control fluid storage, transport, and displacement.

Pore-network architecture and wettability directly control multiphase fluid distribution, displacement sequence, and oil recovery performance in tight porous media. The pore network determines the available flow pathways, coordination number, throat-size hierarchy, and dead-end pore fraction, all of which affect capillary entry pressure, viscous pressure dissipation, and residual-oil trapping (Blunt et al., 2013; Yang et al., 2022). Wettability further determines which phase preferentially occupies small pores, corners, and pore surfaces, thereby influencing capillary pressure, relative permeability, and waterflood breakthrough behavior (Anderson, 1987; Morrow, 1990; Jadhunandan and Morrow, 1995). Recent tight-rock studies have shown that mixed or dual wettability can cause oil and water to occupy different pore-size domains, which strongly influences relative permeability, movable fluid distribution and production performance (Yassin et al., 2016; Javaheri et al., 2018; Liang et al., 2023; Liu et al., 2023). Time-resolved X-ray imaging has directly shown that multiphase displacement proceeds through pore-filling, snap-off, Haines jumps, and intermittent ganglion dynamics, rather than just through a smooth continuum front (Berg et al., 2013; Singh et al., 2017). In-situ wettability measurements and pore-scale flooding experiments further demonstrate that local contact angle, mixed-wet surface distribution, and pore geometry control phase occupancy, displacement pathways, and pore-scale flow regimes (Khishvand et al., 2016; AlRatrout et al., 2017; Scanziani et al., 2017; Rucker et al., 2019). Recent

pore-scale simulations also show that dual wettability and wettability alteration can reorganize flow pathways and change displacement kinetics in natural porous media (Cha et al., 2023; Yang et al., 2024). These observations indicate that pore-size information alone is insufficient, pore connectivity and pore-scale wetting affinity must be characterized and analyzed together to investigate the flow transport behavior of tight rocks.

To precisely and comprehensively characterize the pore-structure of tight rock, a combination of different techniques is necessary because each method probes a different part of the pore system and also has its own limitations. Following the common classification used in unconventional-rock studies, pore-size characterization methods can be grouped into imaging/radiation-based methods and fluid-invasion methods (Bustin et al., 2008; Shi et al., 2019). Mercury injection capillary pressure (MICP) is widely used to quantify connected pore-throat size distributions and capillary entry pressure. However, it primarily reflects mercury-accessible throats and may require extremely high pressure to access nanoscale pores, which could compress or damage tight samples (Al Hinai et al., 2014; Clarkson et al., 2013; Shi et al., 2019). Gas adsorption methods such as N_2 adsorption can resolve mesopores and micropores that are difficult to access by mercury, although they do not directly provide three-dimensional connectivity or flow-path information (Zolfaghari et al., 2017b; Hou et al., 2020). Nuclear magnetic resonance (NMR) can detect connected and isolated pore fluids and evaluate movable-fluid fractions, but the conversion from relaxation time to pore size depends on surface relaxivity, pore geometry, and calibration assumptions (Xiao et al., 2016; Yang et al., 2022). Scanning Electron Microscopy (SEM) and micro-/nano-computed tomography (CT) can directly image pore morphology and extract pore-network parameters, but SEM is limited to two-dimensional fields of view and CT resolution may miss the smallest nanopores in tight sandstones (Bultreys et al., 2016; Lai et al., 2018; Su et al., 2022). Therefore, to accurately and systematically characterize the pore network of tight rocks, a multiscale workflow that combines MICP, gas adsorption, nano-CT, and NMR is needed.

As the fluid distribution and displacement is jointly controlled by pore structure and wettability, wettability-dependent pore characterization is essential. Conventional pore-structure measurements, however, typically provide total pore-size distributions without differentiating water-wet and oil-wet pore domains. In mixed-wet unconventional rocks, different fluids (water and oil) may preferentially access different pores depending on local wettability affinity.

Comparative imbibition behavior of water and oil can therefore be used to infer pore domains with different wetting affinities (Dehghanpour et al., 2013; Lan et al., 2015; Habibi et al., 2016; Yassin et al., 2017). Dehghanpour et al. (2013) showed that comparative brine and oil imbibition in gas shales can reveal water adsorption, microfracturing, and different wetting affinities, while Habibi et al. (2016) used a Montney case study to advance the interpretation of tight-oil wettability. Zolfaghari et al. (2017a, 2017b) used water sorption and N_2 sorption to separate hydrophilic inorganic pores from total pore volume in gas shales, demonstrating that adsorption-based methods can provide wettability-sensitive pore information. Shi et al. (2018, 2019) further proposed an imbibition transient analysis (ITA) method that history matches comparative oil and brine imbibition data with a non-piston-like fractal imbibition model to estimate oil-accessible/water-accessible (organic/inorganic) pore-size distributions. This logic is particularly useful for tight sandstone reservoirs because oil-wet nanoscale pores can retain oil after waterflooding even when larger connected pores are swept by injected water (Javaheri et al., 2018; Liang et al., 2023).

Pore-network modeling (PNM) provides a practical framework for linking experimentally measured pore structure and wettability to multiphase-flow behavior. In a pore-network model, the pore space is represented by connected pore bodies and throats with assigned sizes, conductance, contact angles, and capillary entry pressures, which allows local capillary and viscous controls to be incorporated more explicitly than in continuum-scale models (Blunt et al., 2013; Gostick et al., 2016). Bultreys et al. (2016) reviewed image-based pore-scale transport modeling and emphasized that pore-scale models are most valuable when they are constrained by real pore geometry rather than idealized networks. Berg et al. (2013) used real-time three-dimensional imaging to capture Haines jumps during multiphase flow, providing experimental evidence for the discrete pore-scale events that PNM attempts to represent. Boujelben et al. (2018) used pore-network modeling to investigate low-salinity water injection under unsteady-state conditions and showed that pore-scale wettability changes can affect displacement efficiency. Martinez-Mendoza et al. (2019) estimated capillary pressure and relative permeability for low-salinity waterflooding using pore-network models, highlighting the value of PNM for linking pore-scale interactions to flow functions used in reservoir simulation. Zhao et al. (2019) compared several pore-scale modeling approaches for multiphase flow and showed that model predictions depend strongly on how pore geometry, fluid interfaces, and boundary conditions are represented.

Yang et al. (2022) combined NMR measurements and pore-network simulation to examine how pore structure and injection pressure affect waterflooding in tight oil sandstone cores. Zhang et al. (2022) developed a pore-network model for oil and water transport in mixed-wet nanoporous shale and showed that wettability distribution strongly affects phase transport. X-ray imaging studies on altered-wettability sandstones and mixed-wet reservoir rocks have also provided direct measurements of capillary pressure, relative permeability, and fluid occupancy for comparison with pore-scale model predictions (Lin et al., 2019; Alhammadi et al., 2020; Gao et al., 2020). More recent studies have used pore-scale or pore-network models to evaluate dual wettability, low-salinity waterflooding, pore-filling sequence, and wettability alteration kinetics (Cha et al., 2023; Namaee-Ghasemi et al., 2023; Karimpour Khamaneh and Mahani, 2023; Yang et al., 2024). OpenPNM is an open-source Python platform that allows user-defined networks, pore-scale property assignment, and transport algorithms to be combined in a reproducible workflow (Gostick et al., 2016). Therefore, a mixed-wet OpenPNM model is well suited for this study and can serve as the link between experimental characterization and waterflood/EOR design.

Although pore-structure characterization has been widely applied to tight sandstone reservoirs, few studies have integrated multiple experimental techniques to provide a comprehensive multiscale description of the pore network while also resolving the wettability-dependent pore-size distribution. Moreover, experimental pore-characterization results are not always incorporated into pore-network models that can directly evaluate waterflood performance and provide mechanistic guidance for EOR design. To address this gap, this study develops an integrated multiscale pore-network characterization and modeling workflow for a mixed-wet tight sandstone reservoir. MICP and N_2 adsorption are used to characterize the pore-throat size distribution from micron-scale throats to nanoscale pores, while nano-CT and centrifuge-NMR are used to evaluate pore connectivity and oil mobility. Comparative oil and brine imbibition data are interpreted using ITA to obtain wettability-dependent pore size distributions. The experimental results are then incorporated into an OpenPNM-based mixed-wet pore network model. Pressure controlled waterflood simulations are conducted to evaluate how pore connectivity, oil-water interfacial tension, and pore wettability alteration control water breakthrough, fluid distribution, and oil recovery. By combining experimental characterization with pore-network modeling, this work aims to identify the pore-scale origin of poor waterflood recovery and provide mechanistic

guidance for chemical EOR design in tight sandstone reservoirs. The overall workflow of this study is summarized in **Figure 1**.

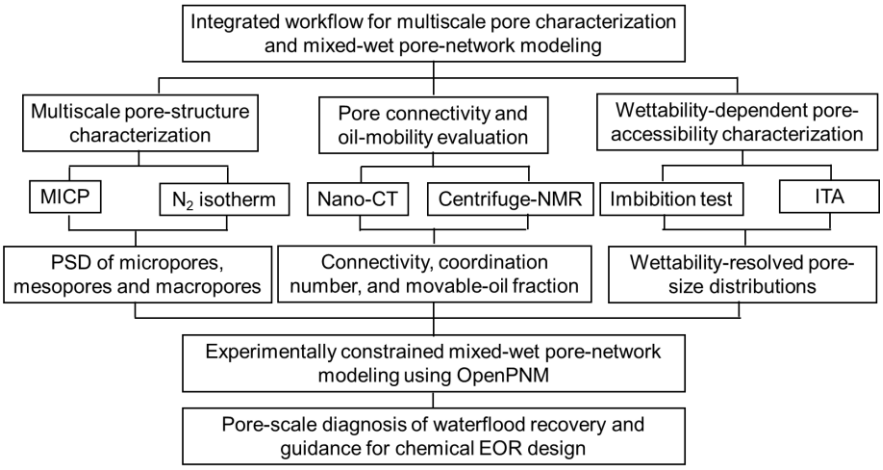

Figure 1 Overall workflow of integrated multiscale pore-network characterization and modeling

Materials and Methods

Materials

In this study, three core samples obtained from a tight sandstone reservoir in middle China were investigated. The basic petrophysical properties of the samples are summarized in **Table 1**. Porosity and gas permeability were measured using standard laboratory procedures. The samples have an average porosity of approximately 15% and gas permeabilities ranging from 1 to 2 mD, which indicates that they are typical low-permeability tight sandstone samples. The temperature of the target reservoir is approximately 50 °C.

Table 2 presents the X-ray diffraction (XRD) results for core sample C-57. The sample is mainly composed of quartz and feldspar minerals. Quartz accounts for approximately 43% of the total mineral content, whereas plagioclase and K-feldspar account for approximately 29% and 8%, respectively. The combined content of these three minerals approaches 80%, indicating a pronounced quartzofeldspathic composition.

Table 1 Physical Properties of the rock samples

Sample ID	Diameter (mm)	Height (mm)	Density (g/cm^3)	Gas Permeability (mD)	Porosity (%)	Measurements
C-57	25.20	65.2	2.23	0.96	14.76	XRD, MICP, N_2 Isotherm, Nano- CT
C-58	25.15	66.3	2.27	1.14	15.19	Centrifuge-NMR
C-60	25.13	63.2	2.28	2.85	15.49	Imbibition Transient Analysis

Table 2 XRD analysis of core C-57

Minerology	Clay	Quartz	K-feldspar	Plagioclase	Calcite	Dolomite	Halite	Anhydrite
Content (%)	7.41	42.60	8.33	28.70	1.72	1.98	1.85	7.41

Crude oil collected from the target reservoir was used in this study. Its density was 0.75 g/cm^3 and viscosity of 1.37 cP at reservoir temperature. The compositions of the crude oil were analyzed by Agilent 7890A Gas Chromatograph and is listed in **Figure 2**. The composition of a recently collected produced-brine sample was analyzed, and the results are summarized in **Table 3**.

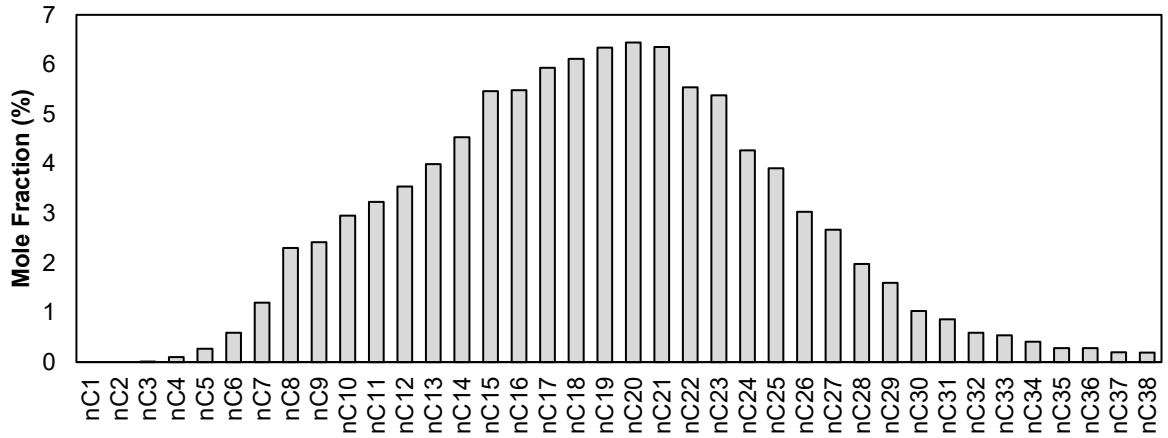

Figure 2 Composition of the crude oil

Table 3 Reservoir brine composition

Composition	Na^+/K^+	Mg^{2+}	Ca^{2+}	Ba^{2+}	Cl^-	HCO_3^-	CO_3^{2-}	Total
Salinity (ppm)	17989	263	15812	1693	57308	52	0	93117

Pore structure characterization

MICP measurement

MICP measurements were conducted using an AutoPore IV 9505 automated mercury porosimeter (Micromeritics, USA) to characterize the pore-throat structure of the tight sandstone sample. Before testing, the sample was dried to remove residual moisture and volatile components, placed in a sealed penetrometer, and evacuated to eliminate air from the pore space and measurement system. Mercury was then progressively injected by increasing the applied pressure, and the cumulative mercury-intrusion volume was recorded at each pressure step. Because mercury is a nonwetting phase, the applied capillary pressure was converted to an equivalent pore-throat radius using the Washburn equation. After reaching the maximum pressure, mercury extrusion was monitored during pressure reduction. The intrusion–extrusion data were used to determine the threshold pressure, pore-throat-size distribution, maximum mercury saturation, and mercury-extrusion efficiency.

N_2 isotherm measurement

Nitrogen adsorption-desorption measurements were conducted at 77 °K to characterize the specific surface area and nanoscale pore size distribution of core samples. The measurements were performed using an ASAP 2460 surface area and porosity analyzer (Micromeritics, USA). Before analysis, the sample was dried and degassed under vacuum to remove residual moisture and volatile components. The equilibrium amount of adsorbed nitrogen was measured over a range of relative pressures (P/P_0), where (P) is the equilibrium nitrogen pressure and (P_0) is the saturation vapor pressure of nitrogen at 77 °K. The specific surface area was determined using the Brunauer–Emmett–Teller (BET) method (Brunauer et al. 1983) over a relative-pressure range of P/P_0=0.05-0.35. The mesopore size distribution was calculated from the adsorption branch over P/P_0=0.35-0.995 using the Barrett–Joyner–Halenda (BJH) method (Barrett et al. 1951), which accounts for capillary condensation and the thickness of the adsorbed film. The low-pressure adsorption data were further analyzed using the Horváth–Kawazoe method (Horváth and Kawazoe, 1983) to estimate the effective pore-size distribution in the micropore range.

Nano-CT measurement

MICP and N_2 isotherm were used to characterize the pore-throat size distribution, specific surface area, and nanopore volume of the tight sandstone. However, these methods do not directly resolve the three-dimensional spatial distribution and connectivity of pores within the rock. Because fluid transport in tight sandstone is controlled not only by pore size but also by pore connectivity, throat continuity, and the development of preferential flow pathways, nano-computed tomography (nano-CT) was further employed to characterize the three-dimensional pore structure.

Sample C-57 was scanned using a NanoVoxel5000 nano-CT. The X-ray tube voltage and current were set to 100 kV and 50 μA, respectively, and the angular increment was 0.1°. A miniature cylindrical specimen was prepared from the core and its surface was carefully polished to minimize image artifacts caused by irregular boundaries. The specimen was mounted at the center of the rotation stage and securely fixed to prevent movement during scanning. Two-dimensional projection images were collected over a full 360° rotation. After scanning, the projection images were corrected and reconstructed to obtain a three-dimensional grayscale volume of the rock sample. The reconstructed dataset was processed using AVIZO software. Image processing included noise reduction, pore–solid segmentation, three-dimensional visualization, and pore-network extraction. Quantitative parameters, including pore number, equivalent pore radius, pore volume, throat length, and connected-pore-volume fraction, were subsequently calculated to evaluate the pore-space geometry and connectivity of the tight sandstone. The voxel size of the reconstructed nano-CT volume was 100 nm. Pores smaller than approximately two to three voxels were not reliably segmented and were therefore not included in the image-based network statistics. Consequently, nano-CT was mainly used to quantify the connectivity of the resolvable pore network, whereas N_2 adsorption and ITA were used to complement the unresolved nanopore-size information.

Centrifuge-NMR measurement

Coupled centrifugation and NMR measurements were conducted to evaluate pore connectivity and the mobility of oil within the target core. Core sample C-58 was first vacuumed and saturated with oil at 20 MPa for 3 days to maximize oil saturation. The oil-saturated core was subsequently aged at 70°C for 2 weeks to restore the reservoir wettability.

The initial transverse relaxation-time (T_2) spectrum of the fully oil-saturated core was measured using a MacroMR12-060H-I NMR analyzer (Niumag, China). The sample was then sequentially centrifuged at 500, 1,000, 2,000, 3,500, 5,000, and 7,000 rpm, with each centrifugation stage lasting 30 minutes. After each stage, NMR measurements were performed to minimize fluid redistribution and evaporation.

At each centrifugal speed, the T_2 spectrum and spin-echo (SE) images were acquired to monitor the redistribution and removal of oil from different pore domains. All NMR acquisition parameters were kept constant throughout the experiments. Changes in the T_2 distributions and SE images were used to evaluate oil mobility, residual-oil distribution, and pore connectivity.

Wettability-dependent pore structure characterization

Traditional characterization techniques, including MICP, N_2 isotherm, and nano-CT, provide information on pore-size distribution, pore geometry, and connectivity but do not directly quantify pore-scale wettability. Wettability is a critical pore-surface property because it governs capillary pressure and, consequently, multiphase-fluid transport, residual-oil distribution, and enhanced oil recovery performance. In our previous work, an ITA method was developed to characterize pore networks with mixed wettability using comparative oil- and brine-imbibition data (Shi et al. 2019). In the ITA workflow, the experimental imbibition curves were first history matched using a non-uniform displacement front spontaneous imbibition model. The model was developed based on the capillary-bundle assumption and fractal theory, which honors the variations in imbibition rate among pores of different sizes (Shi et al. 2018):

$$M_T = \frac{A_f \rho}{2D_{max}^{2-D_f}} \frac{\phi_a'}{1-\left(\frac{D_{min}}{D_{max}}\right)^{2-D_f}} \sqrt{\frac{\sigma cos\theta}{\mu}} \left(\frac{2-D_f}{2.5-D_f}\right) \left[D_C^{2.5-D_f} - D_{min}^{2.5-D_f}\right] \sqrt{t} + \frac{A_f \rho H}{D_{max}^{2-D_f}} \frac{\phi_a}{1-\left(\frac{D_{min}}{D_{max}}\right)^{2-D_f}} \left[D_{max}^{2-D_f} - D_C^{2-D_f}\right] \quad (1)$$

M_T is total imbibed mass of wetting liquid at a certain time. A_f and H are cross-sectional area and height of the rock sample. D_{max} and D_{min} are the maximum and minimum pore diameters, respectively. ρ is the density of wetting liquid. σ is surface tension of wetting liquid and θ is contact angle. Wetting porosity (ϕ_a) is the ratio of the equilibrated volume of imbibed oil or brine (V_{io} or V_{iw}) to V_B and wetting surface porosity (ϕ_a') is the ratio of effective pore area open to oil or

brine imbibition (A_o or A_w) to A_f. D_f is the fractal dimension which controls the PSD. D_C is a time-dependent parameter and decreases with time as smaller pores are filled later than larger pores.

According to the non-piston-like displacement assumption, the equilibrated time (t_{eq}) of the imbibition profile can be interpreted as the time needed for the wetting phase to fill the capillaries with D_{min}. In our previous study (Shi et al. 2018), we developed an equation to calculate D_{min} using t_{eq}:

$$D_{min} = \frac{4\mu(H\tau)^2}{\sigma cos\theta t_{eq}} \tag{2}$$

By history matching the comparative imbibition data, the key unknown parameters such as fractal dimension (D_f) and tortuosity (τ) that control the imbibition process. Then, the determined parameters are utilized to calculate water-invaded pore size distribution (PSD_w) and oil-invaded pore size distribution (PSD_o). Based on the fractal theory, the pore volume fraction of the pores with the diameter from D_1 to D_2 is calculated as (Shi et al. 2019):

$$F(D)\% = \frac{\left(D_2^{2-D_f} - D_1^{2-D_f}\right)}{\left(D_{max}^{2-D_f} - D_{min}^{2-D_f}\right)} \times 100 \tag{3}$$

$F(D)$ is normalized frequency. With the unknown parameters (especially D_{min} and D_f) been determined based on oil and water imbibition data, **Eq. (3)** can then be used to compute PSD_w and PSD_o. In this study, we adopted ITA method to characterize the wettability-dependent pore structure of the target reservoir.

It should be noted that the ITA-derived pore-size distributions represent the pore domains accessible to each imbibing fluid under spontaneous imbibition conditions, rather than a direct image-based segmentation of individual water-wet and oil-wet pores. Therefore, PSDo and PSDw are interpreted as wettability-resolved accessible pore-size distributions. This interpretation is appropriate for constraining the mixed-wet pore-network model, but it does not imply that each pore has a uniquely measured local contact angle.

Pore-network modeling

A two-dimensional mixed-wet pore-network modeling workflow was developed using OpenPNM, an open-source Python framework for constructing pore-network models and solving coupled transport problems. The model was built up with key parameters obtained from prior experimental works, including pore-structure information from MICP, connectivity characteristics from nano-CT image analysis, and wettability-resolved pore-size distributions derived from the ITA method. These experimental inputs were used to define the representative pore-network geometry as well as the distribution of pore elements with different wettability affinity. Water-wet and oil-wet pores were assigned with different contact angles, while throat properties were determined consistently from the connected pore properties and prescribed pore-throat scaling rules.

Waterflooding was simulated with the developed model under pressure-controlled conditions using an implicit pore-network Stokes-flow formulation. The network was initially saturated with oil, and water was injected from the inlet boundary while production was allowed at the outlet boundary. At each pressure step, the pressure field was solved globally by enforcing mass conservation at each pore, and water invasion was evaluated based on the local viscous pressure difference and capillary entry pressure calculated from the Young-Laplace relationship. The invasion process was iterated until no additional pores could be invaded at the imposed pressure, after which the pressure was increased stepwise. The workflow was further applied to evaluate the effects of oil-water interfacial tension and pore wettability alteration on breakthrough behavior, water distribution, and oil recovery.

Results and Discussion

Pore structure characterization

Table 4 summarizes the pore throat structural parameters of the C-57 sample from MICP. **Figure 3** shows the MICP curve and pore-throat size distribution. The maximum, mean, and median pore-throat radius are 2.48, 0.47, and 0.28 μm, respectively, and the pore-throat-size distribution exhibits a modal radius of 0.4 μm with a peak frequency of 11.6%. The sorting coefficient of 2.6 indicates a relatively broad and heterogeneous pore-throat size distribution, whereas the near-zero skewness (0.021) suggests an approximately symmetric distribution. The sample has a threshold pressure of 0.297 MPa and reaches a maximum mercury saturation of 88.69%. The incomplete

mercury intrusion indicates that more than 10% of the pore volume was not accessed within the applied pressure range, likely because of very small pore throats or poorly connected pore space. Therefore, complementary techniques, such as N_2 isotherm, are needed to better characterize the smaller pore networks.

Table 4 Pore-throat structure parameters from MICP

Pore-Throat Radius			Pore-Throat Size Distribution		Sorting Coefficient	Skewness	Kurtosis	Maximum Mercury Saturation (%)	Final Residual Mercury (%)	Threshold Pressure (MPa)
Maximum (μm)	Mean (μm)	Median (μm)	Mode (μm)	Peak Value (%)						
2.475	0.468	0.279	0.400	11.613	2.645	0.021	1.360	88.693	59.031	0.297

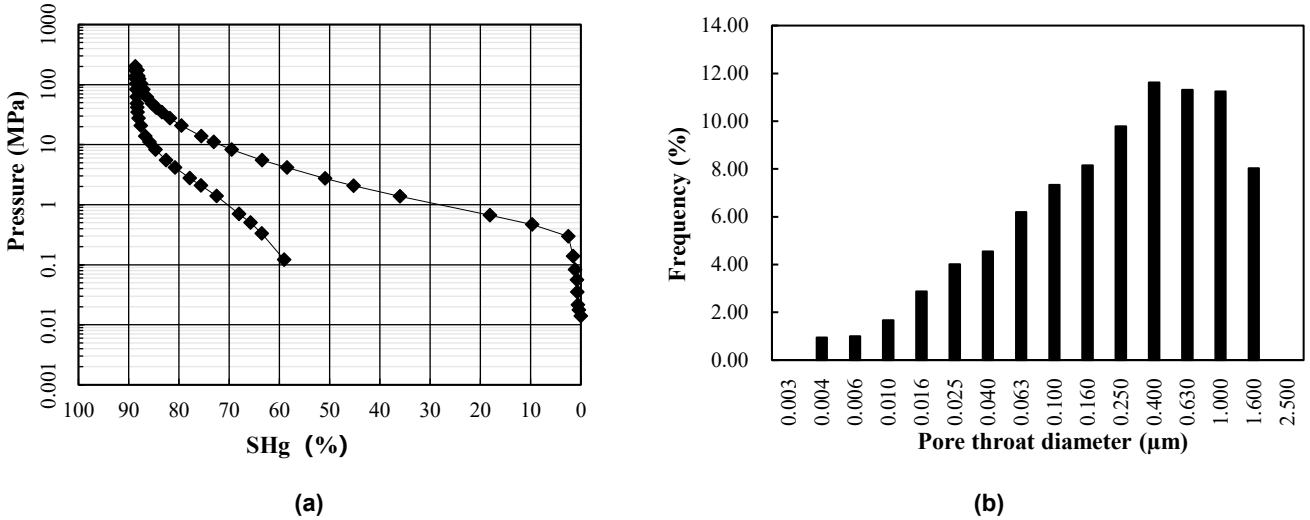

Figure 3 (a) Mercury intrusion capillary pressure curve and (b) pore-throat size distribution

Figure 4 presents the N_2 adsorption–desorption isotherms of Core C-57. According to the International Union of Pure and Applied Chemistry (IUPAC) classification, the isotherm is classified as Type IV, indicating that adsorption is primarily controlled by mesopores. The measured specific surface area and total pore volume are approximately 0.35 m^2/g and 0.0006 cm^3/g, respectively.

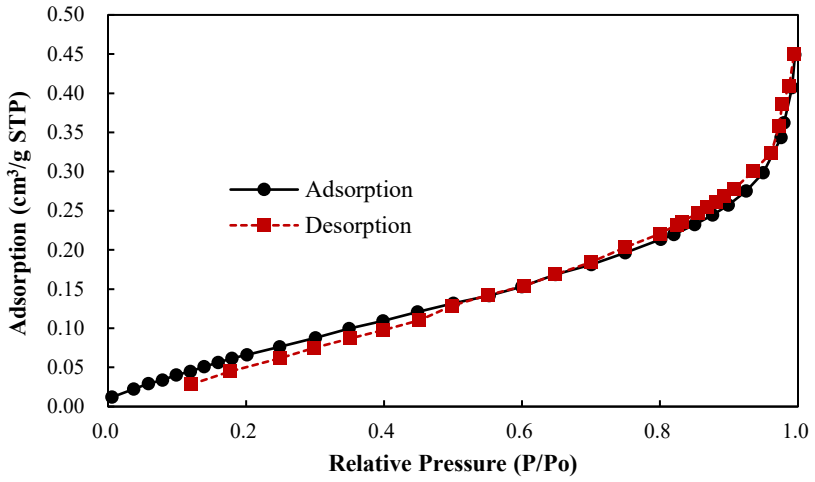

Figure 4 Adsorption–desorption isotherms of core sample C-57

Compared with MICP, N_2 adsorption provides effective characterization of pore size distributions in the mesopore range. The Barrett–Joyner–Halenda (BJH) (Barrett et al. 1951) method is commonly used to determine mesopore-size distributions from gas adsorption–desorption isotherms and to describe capillary condensation in mesopores. In this study, data from the adsorption branch over a relative-pressure range of 0.4~0.9 were used for the BJH analysis to obtain the mesopore-size distribution of Core C-57. The BJH model is based on the Kelvin equation (Thomson 1871)：

$$r_k = -\frac{2\sigma V_m}{RT\ ln(P/P_0)} \tag{4}$$

where r_k is the Kelvin radius, P/P_0 is relative pressure, σ is surface tension, $V_m$is its molar volume, R is the universal gas constant，T is the absolute temperature. Because an adsorbed nitrogen film develops on the pore walls, the actual pore radius (r_p) is obtained by correcting the Kelvin radius (r_k) for the film thickness:

$$r_p = r_k + t \tag{5}$$

where t is the thickness of the adsorbed film. In this study, t was calculated using the Halsey thickness model (Halsey 1948), expressed as:

$$t = 0.534\left(\frac{5}{ln(P/P_0)}\right)^{1/3} \tag{6}$$

Figure 5(a) shows the computed mesopore size distribution by using BJH model. The highest differential pore volume occurs at a pore diameter of about 5.7 nm, with a value of approximately 4.1×10^{-4} cm³/g. Relatively high contributions are also observed at pore diameters below 5 nm. Beyond approximately 6–7 nm, dV/dlogD generally decreases with increasing pore size. The distribution is therefore broad and weakly multimodal, indicating the mesopores are relatively heterogenous.

Kelven equation become less reliable as pore size approaches molecular dimensions, and in this study, the micropore size distributions were determined using the Horváth–Kawazoe (HK) method (Horváth and Kawazoe, 1983). HK method relates the relative equilibrium pressure (mainly P/P_0<0.15) of the adsorbate to the interaction potential, which accounts for the overlapping adsorption potentials generated by opposing pore walls. The original model was developed for nitrogen adsorption at 77.4 K in slit-shaped pores between graphitic carbon layers, which can be adopted here:

$$ln\,(P/P_0) = \frac{62.38}{l-0.64}\left[\frac{1.895\times10^{-3}}{(l-0.32)^3} - \frac{2.7087\times10^{-7}}{(l-0.32)^9} - 0.05014\right] \quad (7)$$

where l is the micropore diameter determined using HK method. **Figure 5(b)** shows the micropore size distribution. The median micropore diameter is approximately 1.62 nm. The distribution is nonuniform and weakly multimodal.

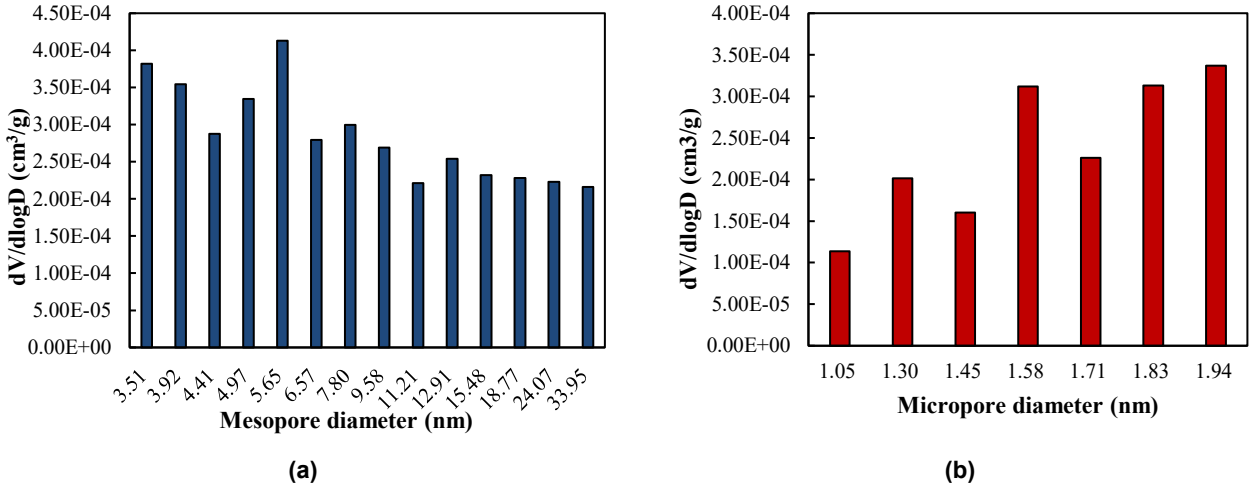

Figure 5 Differential pore-throat volume distribution (dV/dlogD) of (a) mesopores and (b) micropores

Figure 6 shows the three-dimensional reconstructed pore network of C-57 based on the nano-CT scans. The pore system of Core C-57 is highly heterogeneous and poorly connected. The labeled pore structure shows numerous isolated or weakly connected pore clusters, and only 43.80% of the segmented pore volume belongs to the connected pore network. Based on the analysis, the average throat length is approximately 5.91 μm, indicating relatively long and tortuous flow paths between neighboring pores. This combination of limited connectivity, small pore size, and extended throat length restricts fluid transport, which is consistent with the low permeability of the rock sample (K~1 mD).

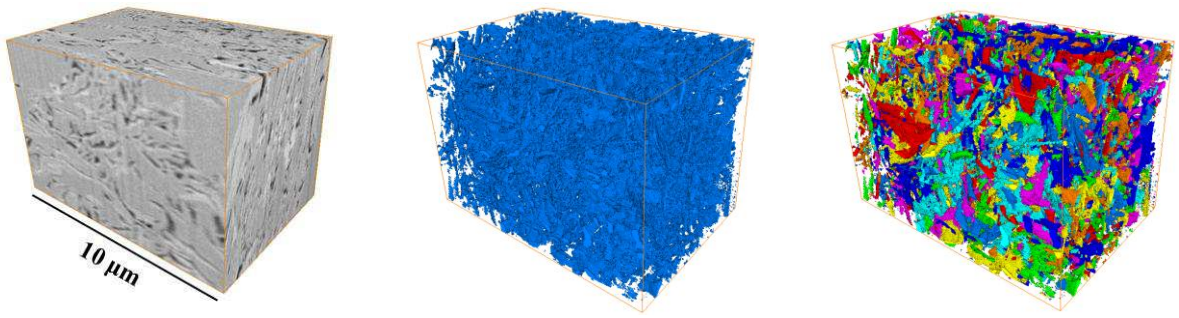

Figure 6 (a) grayscale image, (b) segmented pore space and (c) labeled pore structure of C-57 sample from nano-CT scans

Figure 7 indicates that pores with a coordination number of 1, corresponding to dead-ends, account for 24.7% of the total pore population. These pores are prone to trapping residual oil. Pores with a coordination number of 2, representing chain-like or linearly connected pores, constitute 35.2%. These pores provide limited alternative flow pathways, which results in relatively high flow resistance and increased susceptibility to local flow interruption when an individual throat becomes blocked. Pores with coordination numbers of 1 and 2 account for approximately 60% of the total, partly explains the low waterflood recovery (<15%) of the target reservoir.

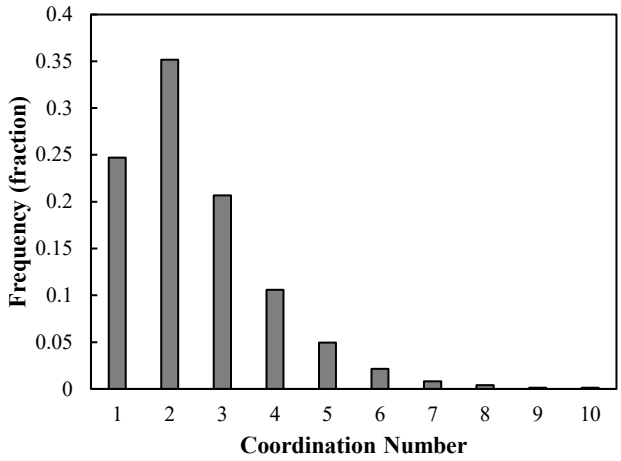

Figure 7 Frequency distribution of pore coordination numbers from micro-CT

Figure 8 compares the T_2 relaxation spectra of Core C-58 before and after stepwise centrifugation. The initially oil-saturated core exhibits a bimodal T_2 distribution, with the dominant peak located at approximately 100 ms. As the centrifugal speed increases from 500 to 7,000 rpm, the overall spectral shape and peak positions remain largely unchanged, whereas only a moderate reduction in signal amplitude is observed. The signal decrease is more pronounced in the longer-T_2 region, which suggests that centrifugation preferentially removes the relatively mobile oil contained in larger or better-connected pores. In contrast, the limited change in the shorter-T_2 region indicates that oil confined in smaller pores is difficult to mobilize. The small incremental reduction in signal at higher centrifugal speeds further suggests that most of the remaining oil is strongly retained by capillary forces. The spin-echo (SE) images in **Figure 9** provide a spatial representation of the oil distribution before and after centrifugations. The overall NMR signal intensity decreases after centrifugation, confirming that part of the oil is expelled from the core. However, the reduction is relatively limited, and strong oil signals remain distributed throughout the sample even after centrifugation at 7,000 rpm. Moreover, the difference between the images obtained at 3,500 and 7,000 rpm is small, indicating limited additional oil removal at the higher centrifugal force. These observations are consistent with the T_2 spectra.

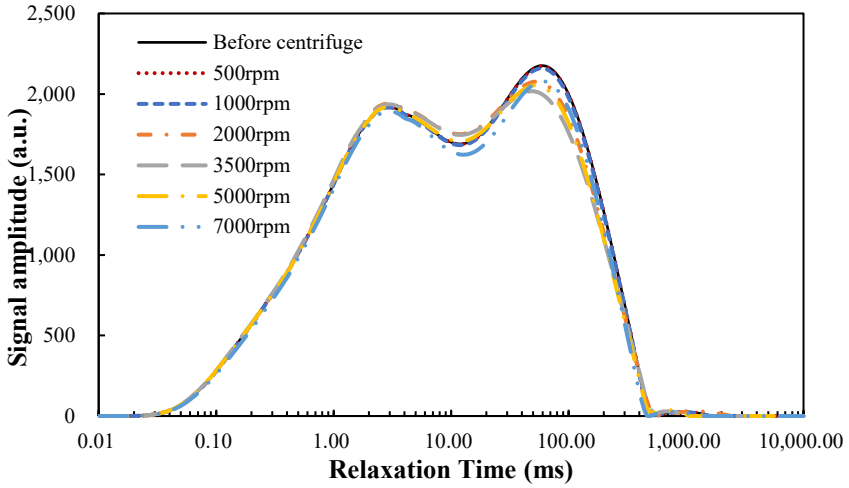

392

393 **Figure 8 T_2 relaxation spectra before and after centrifugation**

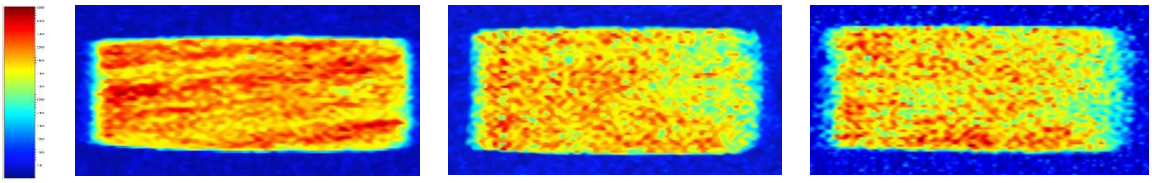

394 **Figure 9 NMR signal intensity maps by SE sequence (a) before centrifuge, (b) 3500rpm centrifuge and (c)**
395 **7000 rpm centrifuge**

396

397 **Table 5** summarizes the stepwise centrifugation conditions, the integrated areas of the T_2 spectra,
398 and the gravimetrically determined oil production. Based on a core-center distance of
399 approximately 0.05 m from the rotational axis, a core length of 66.3 mm, and an oil density of 0.85
400 g/cm³, the equivalent centrifugal pressure difference across the core increased from approximately
401 0.008 MPa at 500 rpm to 1.51 MPa at 7,000 rpm. The integrated T_2 area decreased from 5353.40
402 before centrifugation to 5,122.30 after centrifugation at 7,000 rpm, corresponding to a remaining
403 signal fraction of 95.68%. Based on mass analysis, the core initially contained approximately 3.61
404 g oil, whereas only 0.06 g was cumulatively produced after centrifugation at 7,000 rpm,
405 corresponding to an overall oil recovery factor of 1.69%. Both T_2 spectrum area and mass analysis
406 indicate that only a limited fraction of the oil could be mobilized. The retained oil predominantly
407 resides in small and strongly oil-wet pores. The rotational speed was subsequently increased to
408 9,000 rpm, corresponding to an estimated centrifugal pressure difference of approximately 2.50

MPa. However, slight mechanical damage to the core was observed under this condition, making the corresponding measurements unsuitable for quantitative interpretation. Thus, further increasing the centrifugal force was constrained by the mechanical integrity of the tight sandstone sample.

These results indicate that centrifuge–NMR is effective in demonstrating the limited mobile oil fraction under mechanically safe centrifugal pressures, but it is not sufficient by itself to resolve the full oil-storage pore size distribution in this nanoscale, preferentially oil-wet pore system. The limited oil removal under centrifugation highlights the strong capillary retention of oil and motivates the use of spontaneous imbibition based ITA method to infer the pore domains that are preferentially accessible to oil or brine.

Table 5 Centrifugation conditions, integrated T_2 spectral areas, and oil recovery for Core C-58

Centrifugation stage	Equivalent centrifugal pressure, MPa	Integrated T_2 spectral area	Normalized T_2 spectral area, %	Incremental oil recovery by mass, %
Before centrifuge	0	5353.40	100.00%	0%
500rpm	0.01	5345.24	99.85%	0.41%
1000rpm	0.03	5320.74	99.39%	0.20%
2000rpm	0.12	5298.77	98.98%	0.17%
3500rpm	0.38	5234.21	97.77%	0.28%
5000rpm	0.77	5207.59	97.28%	0.30%
7000rpm	1.51	5122.26	95.68%	0.33%

Wettability-dependence pore structure characterization

Core sample C-60 was cut into two twin plugs, denoted C-60a and C-60b, for comparative brine and oil imbibition experiments. The samples were dried at 80°C until a constant mass was reached, after which their masses were recorded. Each core was then positioned vertically on a mesh support inside a high temperature resistant vessel. The mesh allowed the test fluid to contact only the bottom face of the core while supporting the sample above the vessel base. The experimental system was pre-equilibrated at 50°C. Core C-60a was contacted with brine, and Core C-60b was contacted with crude oil. Co-current spontaneous imbibition was then initiated, and the sample masses were recorded periodically to determine fluid uptake.

Figure 10 presents the imbibed mass as a function of time for the brine and crude oil systems. Both fluids exhibited rapid imbibition during the first 24 hours, suggests the rapid invasion of well-connected relatively large pores. After 24 hours, the brine imbibition rate decreased substantially and quickly approached equilibrium. In contrast, oil imbibition continued for approximately 500 hours before reaching the equilibrium. At equilibrium, crude oil invaded 95.87% of the pore volume, whereas brine invaded only 38.84%. The substantially greater oil uptake, together with the longer oil-imbibition duration, indicates that a larger fraction of the pore volume is preferentially accessible to oil than to brine under spontaneous imbibition conditions. This behavior suggests predominantly oil-wet characteristics, particularly in the smaller pore domains, although the result should be interpreted as a wettability-dependent pore accessibility rather than a direct local contact-angle measurement.

Figure 10 also shows the imbibition profiles modeled by **Eq. (1)**, as shown in the dotted lines. The model inputs, including the core and fluid properties, are summarized in Table 5. The minimum diameter D_{min} was determined from t_{eq} using **Eq. (2)**, and fractal dimension (D_f) and tortuosity (τ) are determined by history matching the experimental data through a global search for the minimum fitting error. The model reproduced both the oil and brine imbibition profiles reasonably well, with R^2 values greater than 0.96. As shown in **Table 6**, the estimated D_{min} for the oil- and brine-invaded pore were 27.8 and 151 nm, respectively. The smaller D_{min} for oil imbibition indicates that the smaller nanoscale pores are preferentially oil-wet. These oil-wet nanopores may retain a considerable amount of crude oil after waterflooding. The oil- and brine-invaded pores exhibited comparable fractal dimensions and tortuosities, which suggests their overall pore structures are not fundamentally different.

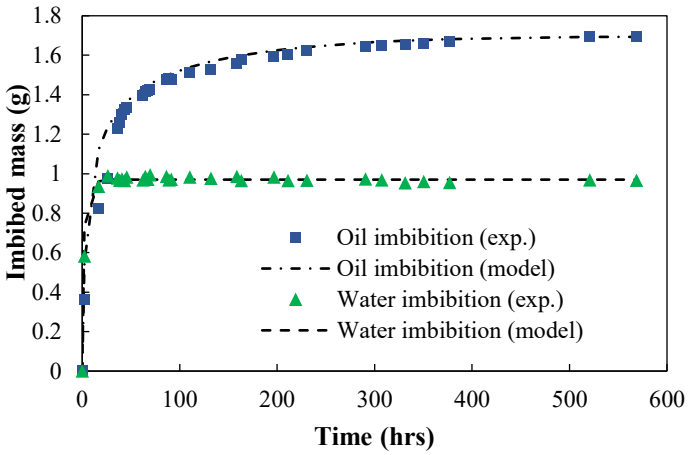

Figure 10 Comparison between measured and modeled brine and oil imbibition for core sample C-60

Table 6 The values of the parameters used and determined in imbibition transient analysis (ITA)

Tests		Oil imbibition test	Water imbibition test
Core Properties	Cross-sectional area, A_f (m^2)	4.91×10^{-4}	4.91×10^{-4}
	Core height, H (m)	0.031	0.033
	Porosity, ϕ (fraction)	0.15	0.15
	Max. diameter, D_{max} (m)	4.95×10^{-6}	4.95×10^{-6}
Fluids properties @50ºC	Viscosity, μ (Pa·s)	1.37×10^{-3}	6.53×10^{-4}
	Density, ρ (Kg/m^3)	749	992
	Surface tension, σ (N/m)	2.07×10^{-2}	6.79×10^{-2}
	Air-liquid contact angle, θ (º)	15.13	47.25
Parameters determined from ITA	Equilibrium time, t_{eq} (s)	34128	1584
	Min. diameter, D_{min} (m)	2.78×10^{-8}	1.51×10^{-7}
	Fractal dimension, D_f	1.95	1.82
	Tortuosity, τ	2.11	2.05

Figure 11 compares the size distribution of the pores invaded by brine imbibition and oil imbibition. As shown in the figure, oil-invaded pores cover a wider size range, with a minimum pore diameter of 0.018 μm. Approximately 19% of the oil-invaded pore volume is associated with mesopores (2–50 nm), whereas the remaining 81% is contributed by macropores (>50 nm). In comparison, the minimum diameter of the water-invaded pores is 0.151 μm, and all water-invaded pores fall within the macropore range. The mean and median pore diameters are also larger for the water-invaded pores, reaching 1.608 and 1.157 μm, respectively, compared with 0.970 and 0.367 μm for the oil-invaded pores. These results indicate that the smaller nano scale pores are more oil-

wet. It is worth noting that pores accessed during oil imbibition account for 95.9% of the total pore volume. Because the combined pore volume fractions accessed by oil and water imbibition exceed 100%, substantial overlap must exist. This overlap indicates that a large fraction of the pore space can imbibe both oil and brine, and therefore be considered mixed-wet.

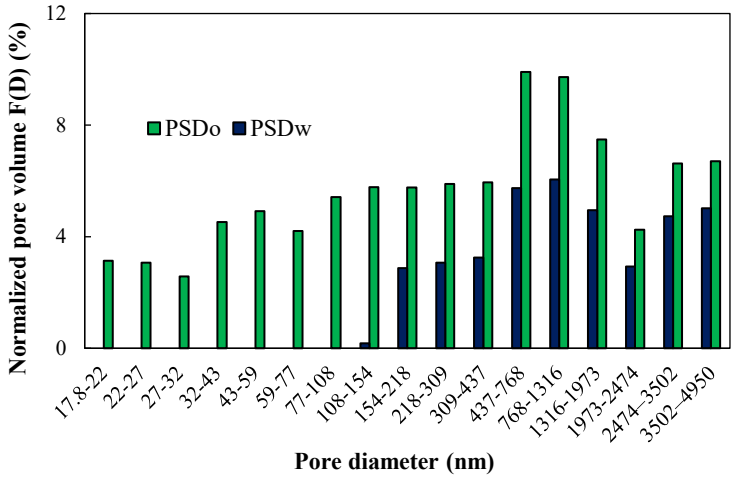

Figure 11 Comparison between pore size distributions by oil imbibition (PSDo) and brine imbibition (PSDw)

The ITA method enables a more detailed characterization of wettability-dependent pore-size distributions, which is important for evaluating EOR potential. After secondary waterflood, the target reservoir achieved an oil recovery of less than 20%, which indicates that a substantial amount of oil remained trapped within the tight pore network. This residual oil is expected to be concentrated particularly in oil-wet nanoscale pores, where strong capillary forces hinder oil displacement. Mobilizing oil from these regions is therefore a primary objective of the subsequent EOR process. In the following section, preliminary pore-network modeling was conducted using the pore structure information obtained above to identify the key parameters that should be targeted during chemical EOR.

Waterflood modeling with OpenPNM

In this section, a two-dimensional mixed-wet pore-network model was generated using structural and wettability information obtained from MICP, nano-CT, and ITA analysis. The model size was set to 100 μm × 100 μm, with an effective thickness of 100 μm for pore and throat volume calculations. As shown in **Figure 12**, the reference network was constructed with a mean coordination number of 2.31 and a median coordination number of 2.0, consistent with the nano-

CT results in **Figure 7**. The total porosity, including pores and throats, was scaled to 15%. To avoid artificial boundary flow, throats along the model boundaries were removed before flow simulation.

The hydrophilic and lipophilic pore-size distributions obtained from ITA were treated as pore-body diameter distributions. Pore bodies rather than throats were considered to control the imbibition process (Shi et al. 2019). Throat diameters were therefore calculated using a fixed throat-to-pore diameter ratio of 0.55. The network was uniformly scaled until the total pore and throat volume matched the target porosity of 15% listed in **Table 1**. The final reference network contained 30,000 pores and 37,651 throats. Based on the PSD obtained by ITA in **Figure 11**, the network included 265 hydrophilic pores and 29,735 oil-wet pores. Although the number fraction of hydrophilic pores is small, these pores correspond to the larger pore-size bins in PSD_w and therefore account for a disproportionately large pore volume. This assignment is consistent with the ITA result that brine primarily accesses larger macropores, whereas oil accesses both macropores and smaller nanoscale pores. Hydrophilic and lipophilic pores were assigned contact angles of 30° and 150°, respectively. Throat contact angles were calculated as the arithmetic mean of the two connected pore contact angles, and throats connecting pores with different wettability states were defined as mixed-wet throats. This network served as the base case for subsequent IFT and wettability sensitivity analyses. For the wettability sensitivity analysis, a cumulative random fraction of initially oil-wet pores was converted to water-wet pores to isolate the effect of wettability state on water accessibility. This treatment does not represent the spatially resolved transport and adsorption of a specific chemical agent. Instead, it provides an upper-bound and mechanism-oriented analysis of how the recovery would respond if different fractions of oil-wet pore domains became water-accessible after chemical treatment.

The model should be interpreted as a physically constrained conceptual pore network rather than a direct voxel-to-network extraction of the scanned CT volume. Its purpose is to evaluate the relative effects of connectivity, IFT, and wettability distribution under experimentally constrained pore-size and coordination-number statistics.

512 **Table 7. Key parameters used in the OpenPNM reference model**

Parameter	Value	Experimental basis
Model size	100 μm × 100 μm × 100 μm	representative pore-network domain
Porosity	15%	core porosity
Mean coordination number	2.31	nano-CT
Median coordination number	2.0	nano-CT
Number of pores	30,000	network construction
Number of throats	37,651	network construction
Pore-size distribution	PSDo / PSDw	ITA method
Throat-to-pore diameter ratio	0.55	model assumption
Water-wet contact angle	30°	assumed strongly water-wet
Oil-wet contact angle	150°	assumed strongly oil-wet
IFT range	30–0.0003 mN/m	waterflood to ultralow-IFT surfactant flooding

513

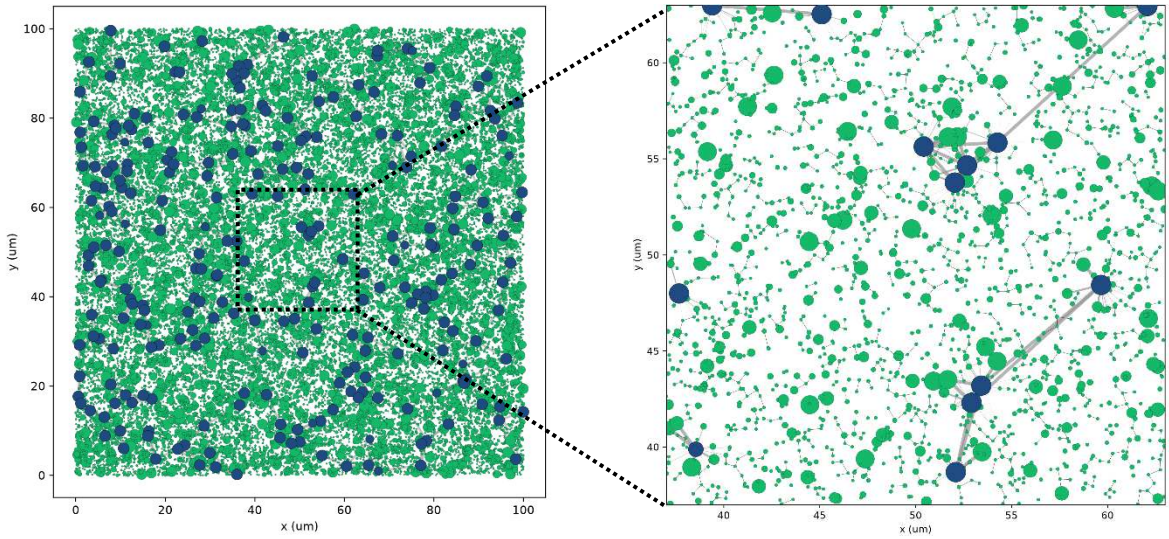

514 **Figure 12 Two-dimensional mixed-wet reference pore network model used for waterflood simulations. Green,**
515 **blue, and gray denote oil-wet pores, water-wet pores, and throats, respectively.**

516 Waterflood was simulated using an implicit pore-network Stokes flow model. For each imposed
517 pressure difference, the pressure field was solved globally over the network by enforcing mass
518 conservation at each pore. Simulations were conducted at 50ºC, using the brine and oil density and
519 viscosity values listed in **Table 6**. The inlet was defined as pores in the upper-left corner of the
520 network, whereas the outlet was defined as pores in the lower-right corner. A constant-pressure
521 boundary condition was applied, with the outlet pressure fixed at zero and the inlet pressure
522 increased stepwise. The network was initially oil-saturated, except for the inlet pores, which were
523 assigned as water-filled. At each pressure step, the pressure field was solved implicitly, and water

524 invasion was evaluated at all oil–water interfacial throats according to the Young–Laplace
525 equation. A neighboring oil-filled pore was invaded when the local water phase pressure drop
526 across the connecting throat exceeded its capillary entry pressure. The pressure solution and
527 invasion update were repeated within each pressure step until no further pores were invaded. To
528 guide chemical design for the target reservoir, oil-water IFT and pore wettability were varied to
529 evaluate their potential effects on oil recovery efficiency.

530 ***Effect of IFT***

531 In this section, the reference mixed-wet network shown in **Figure 12** was used to evaluate the
532 effect of IFT. The IFT was varied logarithmically from 30 to 0.0003 mN/m, while the network
533 geometry and wettability distribution were kept unchanged. This range represents conditions from
534 conventional waterflood (IFT ~ 30 mN/m) to surfactant flooding that can develop ultralow IFT
535 (<0.003 mN/m). For each IFT case, the pressure difference was increased from 0 to 20 MPa in
536 increments of 0.5 MPa. The imposed pressure difference was not intended to represent a field-
537 scale pressure gradient. Instead, it was used as a controlled numerical parameter to probe the
538 capillary entry threshold of the experimentally constrained pore network. The low pressure cases
539 are used to represent realistic waterflooding tendencies, whereas the high pressure cases provide
540 an upper bound assessment of whether pressure increase alone can overcome capillary trapping in
541 oil-wet nanoscale pores.

542 **Figure 13** compares the fluid distributions after waterflood (IFT=30 mN/m) and ultralow-IFT
543 flooding (IFT=0.0003 mN/m) at low and high pressure drops. As shown in **Figure 13(a)**, under
544 low-pressure waterflood, injected water preferentially channels through connected hydrophilic
545 pathways and quickly reaches the outlet, resulting in early breakthrough and relatively low oil
546 recovery of approximately 48%. Even when the pressure difference is increased, as shown in
547 **Figure 13(b)**, oil recovery does not improve because water continues to flow through the
548 preferential channels. This behavior is consistent with field observations in the target reservoir,
549 where early water breakthrough and low secondary recovery by waterflooding were observed.
550 When ultralow IFT is achieved, more oil can be displaced from smaller pores, improving oil
551 recovery to approximately 53%, as shown in **Figure 13(c)**. As the pressure difference further
552 increases up to 10 MPa, water can invade more nanoscale pores, and oil recovery increases to
553 approximately 58% (**Figure 13(d)**).

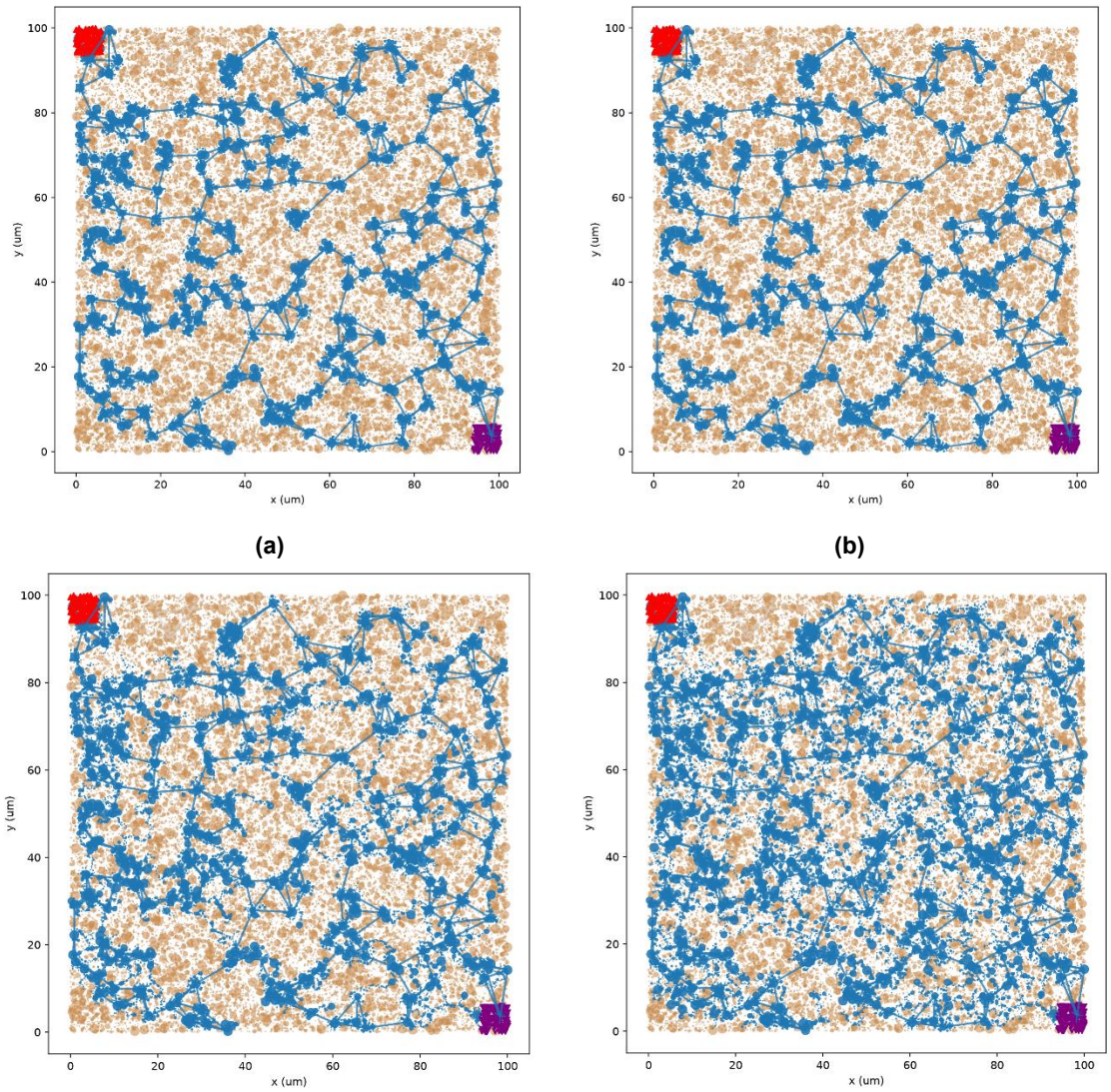

Figure 13 Oil–water distributions after waterflood under IFT=30 mN/m at (a) ΔP = 1 MPa and (b) ΔP = 10 MPa, and under IFT=0.0003 mN/m at (c) ΔP = 1 MPa and (d) ΔP = 10 MPa. Brown, blue, red, and purple denote oil, water, inlets, and outlets, respectively.

Figure 14 further summarizes the six IFT cases. **Figure 14(a)** compares oil recovery as a function of pressure drop for IFT values ranging from 30 to 0.0003 mN/m. At relatively high IFT values (>0.1 mN/m), increasing pressure has a negligible effect on oil recovery. Further reduction in IFT leads to improved recovery, with recovery factors increasing to approximately 49.6%, 54.6%, and 61.9% at IFT values of 0.03, 0.003, and 0.0003 mN/m, respectively. **Figure 14(b)** compares oil recovery as a function of IFT at selected pressure drops of 0.5, 2.5, 5, 10, and 20 MPa. The results show that increasing pressure improves oil recovery only when the IFT is reduced below 0.03

mN/m. As illustrated in **Figure 13**, at high IFT, water preferentially flows through the connected hydrophilic pathways and bypasses a large fraction of the oil-wet regions; therefore, increasing pressure alone provides limited additional recovery. As IFT decreases, capillary barriers in smaller or less favorable throats are reduced, allowing water to access additional pore clusters and improving microscopic sweep efficiency.

However, even under an unrealistically high pressure drop of 20 MPa across the small network model, oil recovery increases only from 48.7% at 30 mN/m to 61.9% under ultralow-IFT conditions (<0.001 mN/m). This indicates that reducing IFT alone is insufficient to recover a substantial portion of residual oil in such mixed-wet tight porous media. Additional mechanisms, such as wettability alteration, may therefore be required to further improve oil recovery.

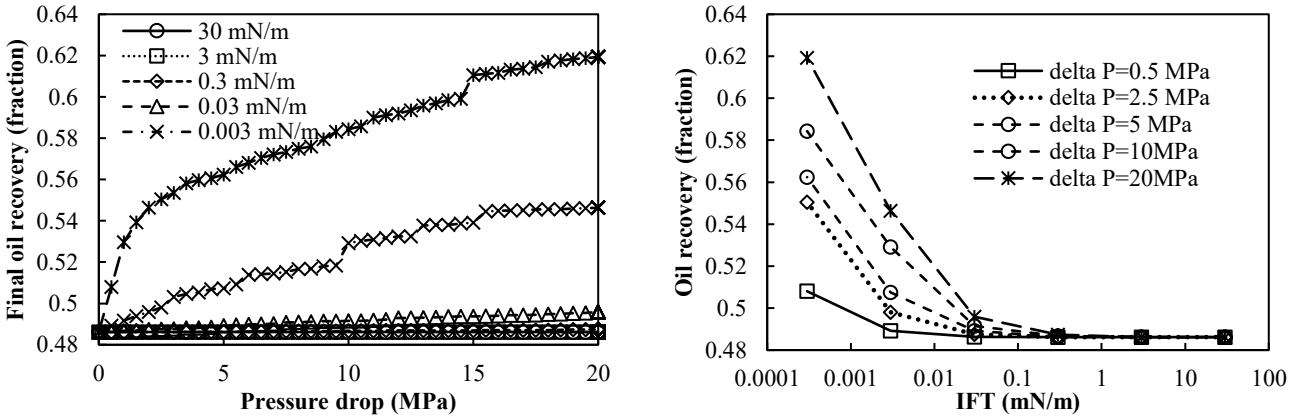

(a) (b)

Figure 14 (a) Oil recovery vs. IFT at various pressure drops and (b) oil recovery vs. pressure drop at various IFT conditions

Effect of wettability

The wettability-conversion sensitivity cases were performed using the same reference network geometry. The tested conversion fractions were 20%, 40%, 60%, 80%, and 100% of the original oil-wet pores. For each case, the selected oil-wet pores were reassigned a water-wet contact angle of 30°, and throat contact angles were recalculated based on the updated wettability states of the connected pores. Waterflooding was then simulated at an IFT of 30 mN/m and a constant pressure drop of 0.5 MPa. This analysis was used to preliminarily assess how pore wettability affects waterflooding performance.

Figure 15 compares the fluid distributions after waterflood under the six wettability conditions. As more lipophilic pores were converted to hydrophilic pores, the microscopic sweep efficiency improved significantly. For example, when 20% of the lipophilic pores were converted, approximately 52.3% of the pore volume was invaded by water (**Figure 15(b)**). When the conversion fraction increased to 80%, more than 85% of the pore volume was invaded (**Figure 15(e)**).

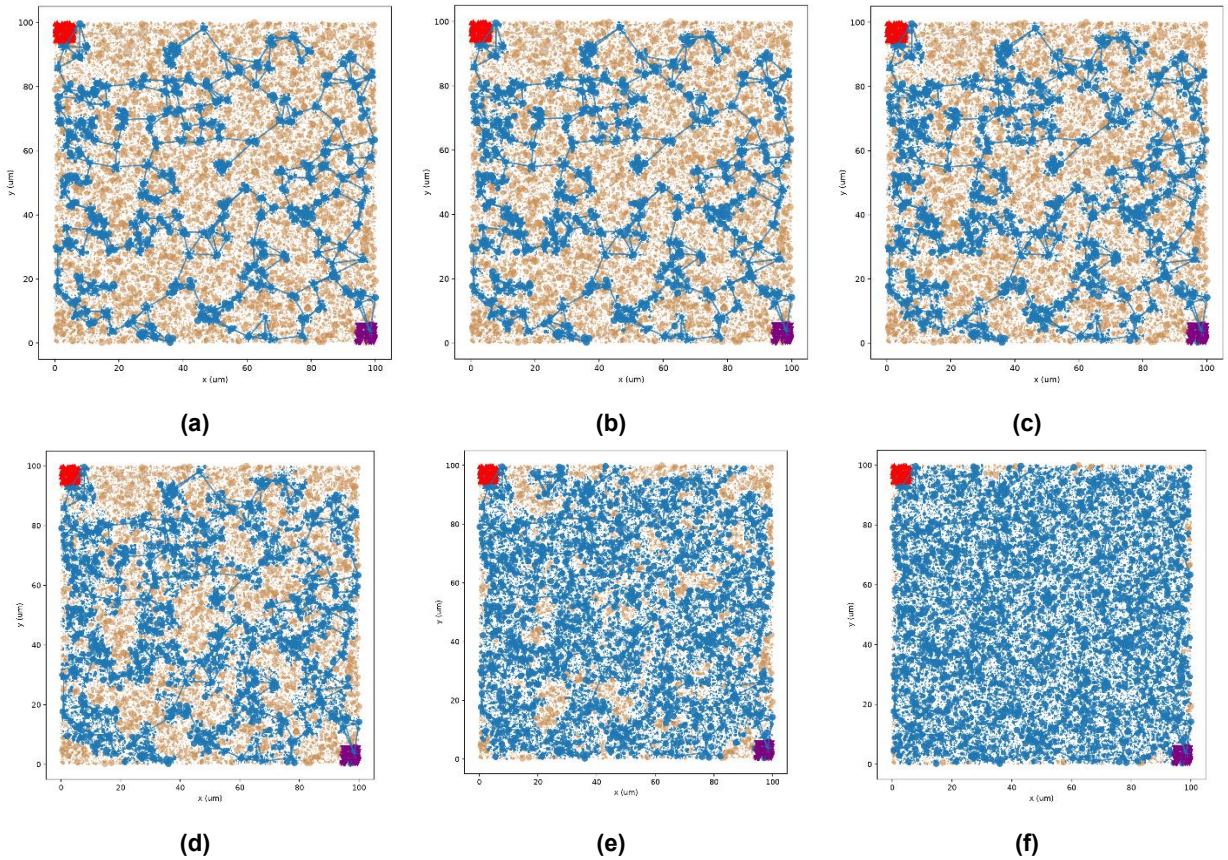

Figure 15 Oil–water distributions after waterflooding at ΔP = 0.5 MPa and IFT = 30 mN/m under different wettability conditions: (a) reference mixed-wet network; (b) 20%, (c) 40%, (d) 60%, (e) 80%, and (f) 100% of oil-wet pores converted to water-wet pores.

Figure 16 compares oil recovery during low-pressure waterflood for the same network under different wettability conditions. Oil recovery increased substantially as more oil-wet pores were converted to water-wet pores. When 20% of the original oil-wet pores were converted, the final recovery factor reached 52.3%. Recovery further increased to 55.2% and 62.0% for 40% and 60% conversion, respectively. A more pronounced improvement was observed at 80% conversion, where the final recovery factor increased to 85.8%. When all originally oil-wet pores were

converted to water-wet pores, the final recovery factor reached 95.7%. Compared with the maximum recovery of 61.9% achieved in the reference pore network under ultralow-IFT condition (0.0003 mN/m) and high pressure (20 MPa), these results highlight the critical role of wettability alteration in tight mixed-wet reservoirs. Chemical formulations that significantly reduce IFT but do not alter wettability may therefore provide limited incremental oil recovery. These results provide an important screening criterion for future chemical EOR design in the target reservoir.

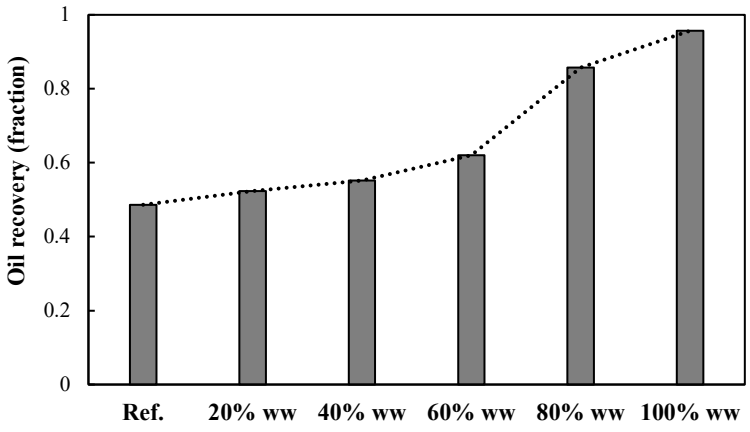

Figure 16 Oil recovery for different wettability conditions after 0.5 MPa delta P waterflood. Note: ww denotes the fraction of originally oil-wet pores converted to water-wet pores.

It should be noted that chemical-induced wettability alteration occurs only in chemically contacted pores, rather than randomly throughout the network. More detailed dynamic wettability alteration modeling can be performed using CMG, ECLIPSE, or in-house simulators that explicitly account for wettability alteration mechanisms (Shi et al., 2024). Here, the analysis is intended to isolate the effect of pore wettability and provide preliminary guidance for chemical EOR design over the target reservoir.

Conclusions

This study developed an integrated workflow combining multiscale pore-structure characterization, wettability-dependent pore size distribution (PSD) analysis and the pore-network modeling to investigated waterflooding performance in a tight sandstone reservoir. MICP, N_2 adsorption, nano-CT and centrifuge-NMR tests were conducted on reservoir cores to characterize pore structure and connectivity. Competitive imbibition were then conducted on twin samples to investigate the

wettability-dependent PSD by using the imbibition transient analysis (ITA) method. The experimentally derived pore-structure and wettability information was subsequently incorporated into an OpenPNM-based mixed-wet pore-network model to evaluate the waterflooding performance and to examine how pore connectivity, oil–water IFT, and wettability alteration affect fluid displacement and oil recovery. The key findings are summarized as follows:

1. The target tight sandstone contains a heterogeneous pore-throat system with both micron-scale pore throats and abundant nanoscale pores. MICP characterized the larger pore-throat network, whereas N_2 adsorption provided complementary information on mesopores and micropores that cannot be fully resolved by mercury intrusion.

2. Nano-CT analysis indicates that the pore system is poorly connected. A large fraction of the segmented pore volume is isolated or weakly connected, and pores with coordination numbers of 1 and 2 dominate the network. This limited connectivity provides a pore-scale explanation for the low permeability and low secondary waterflood recovery observed in the target reservoir.

3. Centrifuge-NMR measurements show that only a limited amount of oil can be mobilized even as the centrifugal pressure is increased. The retained oil is mainly associated with small and poorly connected oil-wet pores, where capillary forces and unfavorable wettability make oil removal difficult.

4. The ITA results demonstrate that the rock is predominantly oil-wet. The estimated minimum pore diameter was approximately 27.8 nm for oil-invaded pores and 151 nm for brine-invaded pores, indicating that smaller nanoscale pores are preferentially oil-wet and are likely to retain residual oil after waterflooding.

5. OpenPNM simulations based on the experimentally constrained mixed-wet network show that water preferentially channels through connected water-wet pathways and bypasses many oil-wet pore clusters. Lowering oil-water IFT improves recovery by reducing capillary entry barriers, but the improvement remains limited when the pore network remains predominantly oil-wet.

6. Within the experimentally constrained mixed-wet network, wettability alteration has a stronger effect on simulated oil recovery than IFT reduction alone. As more oil-wet pores are converted

to water-wet pores, the accessible water-flow network expands and microscopic sweep efficiency increases significantly. These results suggest that effective chemical EOR design for the target reservoir should combine IFT reduction with sufficient wettability alteration, especially in oil-wet nanoscale pore domains where residual oil is strongly retained.

The present pore-network model is a 2D, statistically constrained representation of the pore system, and the wettability-conversion cases were designed as mechanistic sensitivity analyses rather than direct simulations of chemical transport. Future work should couple pore-scale chemical transport, adsorption, and dynamic wettability alteration with three-dimensional image-based networks to predict which oil-wet pore domains can be contacted and altered during actual chemical flooding.

Acknowledgments

This study is funded by the Oil & Gas Major Project (No.2025ZD1406200). This work was also supported by the National Science Foundation of China (NSFC) grant U25B20128, grant 52304050 and grant 23FAA01777.

References

Al Hinai, A., Rezaee, R., Esteban, L., & Labani, M. (2014). Comparisons of pore size distribution: A case from the Western Australian gas shale formations. Journal of Unconventional Oil and Gas Resources, 8, 1-13.

Anderson, W. G. (1987). Wettability literature survey-Part 6: The effects of wettability on waterflooding. Journal of Petroleum Technology, 39(12), 1605-1622. https://doi.org/10.2118/16471-PA

Barrett, E. P., Joyner, L. G., & Halenda, P. P. (1951). The determination of pore volume and area distributions in porous substances. I. Computations from nitrogen isotherms. Journal of the American Chemical society, 73(1), 373-380.

Blunt, M. J., Bijeljic, B., Dong, H., Gharbi, O., Iglauer, S., Mostaghimi, P., Paluszny, A., & Pentland, C. (2013). Pore-scale imaging and modelling. Advances in Water Resources, 51, 197-216. https://doi.org/10.1016/j.advwatres.2012.03.003

Boujelben, A., McDougall, S., Watson, M., Bondino, I., & Agenet, N. (2018). Pore network modelling of low salinity water injection under unsteady-state flow conditions. Journal of Petroleum Science and Engineering, 165, 462-476. https://doi.org/10.1016/j.petrol.2018.02.040

Brunauer, S., Emmett, P. H., & Teller, E. (1938). Adsorption of gases in multimolecular layers. Journal of the American chemical society, 60(2), 309-319.

680 Bustin, R. M., Bustin, A. M. M., Cui, X., Ross, D. J. K., & Pathi, V. M. (2008). Impact of shale
681 properties on pore structure and storage characteristics. SPE Shale Gas Production Conference.
682 SPE-119892-MS.

683 Cha, L., Feng, Q., Wang, S., Xu, S., & Xie, C. (2023). Pore-scale modeling of immiscible
684 displacement in porous media: The effects of dual wettability. SPE Journal, 28(1), 239-250.
685 https://doi.org/10.2118/210589-PA

686 Gostick, J., Aghighi, M., Hinebaugh, J., Tranter, T., Hoeh, M. A., Day, H., Spellacy, B., Sharqawy,
687 M. H., et al. (2016). OpenPNM: A pore network modeling package. Computing in Science &
688 Engineering, 18(4), 60-74. https://doi.org/10.1109/MCSE.2016.49

689 Halsey, G. (1948). Physical adsorption on non-uniform surfaces. The Journal of chemical physics,
690 16(10), 931-937.

691 Horváth, G., & Kawazoe, K. (1983). Method for the calculation of effective pore size distribution
692 in molecular sieve carbon. Journal of Chemical Engineering of Japan, 16(6), 470-475.

693 Hou, X., Zhu, Y., Chen, S., Wang, Y., & Liu, Y. (2020). Investigation on pore structure and
694 multifractal of tight sandstone reservoirs in coal bearing strata using LF-NMR measurements.
695 Journal of Petroleum Science and Engineering, 187, 106757.
696 https://doi.org/10.1016/j.petrol.2019.106757

697 International Energy Agency. (2023). World Energy Outlook 2023. IEA.
698 https://www.iea.org/reports/world-energy-outlook-2023

699 Jadhunandan, P. P., & Morrow, N. R. (1995). Effect of wettability on waterflood recovery for
700 crude-oil/brine/rock systems. SPE Reservoir Engineering, 10(1), 40-46.
701 https://doi.org/10.2118/22597-PA

702 Javaheri, A., Habibi, A., Dehghanpour, H., & Wood, J. M. (2018). Imbibition oil recovery from
703 tight rocks with dual-wettability behavior. Journal of Petroleum Science and Engineering, 167,
704 180-191. https://doi.org/10.1016/j.petrol.2018.01.046

705 Karimpour Khamaneh, M., & Mahani, H. (2023). Pore-scale insights into the nonmonotonic effect
706 of injection water salinity on wettability and oil recovery in low-salinity waterflooding. Energy &
707 Fuels, 37(19), 14764-14777. https://doi.org/10.1021/acs.energyfuels.3c02603

708 Lai, J., Wang, G., Wang, Z., Chen, J., Pang, X., Wang, S., Zhou, Z., He, Z., et al. (2018). A review
709 on pore structure characterization in tight sandstones. Earth-Science Reviews, 177, 436-457.
710 https://doi.org/10.1016/j.earscirev.2017.12.003

711 Lan, Q., Dehghanpour, H., Wood, J., & Sanei, H. (2015). Wettability of the Montney tight gas
712 formation. SPE Reservoir Evaluation & Engineering, 18(3), 417-431.
713 https://doi.org/10.2118/171620-PA

714 Liang, C., Xiao, L., Jia, Z., Guo, L., Luo, S., & Wang, Z. (2023). Mixed wettability modeling and
715 nuclear magnetic resonance characterization in tight sandstone. Energy & Fuels, 37(3), 1962-1974.
716 https://doi.org/10.1021/acs.energyfuels.2c03720

Liu, G., Wang, H., Tang, J., Liu, Z., & Yang, D. (2023). Effect of wettability on oil and water distribution and production performance in a tight sandstone reservoir. Fuel, 341, 127680. https://doi.org/10.1016/j.fuel.2023.127680

Martinez-Mendoza, E. G., Diaz-Viera, M. A., Coronado, M., & Mendoza-Rosas, A. T. (2019). Capillary pressure and relative permeability estimation for low salinity waterflooding processes using pore network models. Journal of Petroleum Science and Engineering, 182, 106253. https://doi.org/10.1016/j.petrol.2019.106253

Morrow, N. R. (1990). Wettability and its effect on oil recovery. Journal of Petroleum Technology, 42(12), 1476-1484. https://doi.org/10.2118/21621-PA

Namaee-Ghasemi, A., Ayatollahi, S., & Mahani, H. (2023). Insights into the effects of pore structure, time scale, and injection scenarios on pore-filling sequence and oil recovery by low-salinity waterflooding using a mechanistic DLVO-based pore-scale model. SPE Journal, 28(4), 1760-1776. https://doi.org/10.2118/214320-PA

Shi, Y., Mohanty, K. K., Leung, J. Y., & You, Q. (2024). A New Mechanistic Model for Wettability-Altering Surfactant Floods in Carbonates. SPE Journal, 29(05), 2672-2685.

Shi, Y., Yassin, M. R., & Dehghanpour, H. (2018). A modified model for spontaneous imbibition of wetting phase into fractal porous media. Colloids and Surfaces A: Physicochemical and Engineering Aspects, 543, 64-75.

Shi, Y., Yassin, M. R., Yuan, L., & Dehghanpour, H. (2019). Modelling imbibition data for determining size distribution of organic and inorganic pores in unconventional rocks. International Journal of Coal Geology, 201, 26-43. https://doi.org/10.1016/j.coal.2018.11.010

Su, Y., Zha, M., Jiang, L., Ding, X., Qu, J., Jin, J., & Iglauer, S. (2022). Pore structure and fluid distribution of tight sandstone by the combined use of SEM, MICP and X-ray micro-CT. Journal of Petroleum Science and Engineering, 208, 109241. https://doi.org/10.1016/j.petrol.2021.109241

Thomson, W. (1872). 4. On the equilibrium of vapour at a curved surface of liquid. Proceedings of the Royal Society of Edinburgh, 7, 63-68.

U.S. Energy Information Administration. (2013). Technically recoverable shale oil and shale gas resources: An assessment of 137 shale formations in 41 countries outside the United States. U.S. EIA.

Xiao, L., Zou, C., Mao, Z., Jin, Y., Shi, Y., Guo, H., & Li, G. (2016). An empirical approach of evaluating tight sandstone reservoir pore structure in the absence of NMR logs. Journal of Petroleum Science and Engineering, 137, 227-239. https://doi.org/10.1016/j.petrol.2015.11.035

Yang, Y., Li, H., Tong, C., Zhang, L., Sun, H., Zhong, J., Zhang, K., & Yao, J. (2024). Pore-scale simulation of the effect of wettability alteration on flow transport kinetics in 3D natural porous media. SPE Journal, 29(11), 6332-6349. https://doi.org/10.2118/223106-PA

Yang, Y., Xiao, W., Bernabe, Y., Xie, Q., Wang, J., He, Y., Li, M., & Chen, M. (2022). Effect of pore structure and injection pressure on waterflooding in tight oil sandstone cores using NMR technique and pore network simulation. Journal of Petroleum Science and Engineering, 217, 110886. https://doi.org/10.1016/j.petrol.2022.110886

Yassin, M. R., Begum, M., & Dehghanpour, H. (2017). Organic shale wettability and its relationship to other petrophysical properties: A Duvernay case study. International Journal of Coal Geology, 169, 74-91. https://doi.org/10.1016/j.coal.2016.11.015

Zhang, T., Javadpour, F., Li, J., Zhao, Y., Zhang, L., & Li, X. (2021). Pore-scale perspective of gas/water two-phase flow in shale. SPE Journal, 26(2), 828-846. https://doi.org/10.2118/205019-PA

Zhang, W., Feng, Q., Wang, S., Zhang, J., Jin, Z., Xia, T., Xing, X., & Lv, P. (2022). Pore network modeling of oil and water transport in nanoporous shale with mixed wettability. Journal of Petroleum Science and Engineering, 209, 109884. https://doi.org/10.1016/j.petrol.2021.109884

Zhao, W., Hu, S., Hou, L., Yang, T., Li, X., Guo, B., & Yang, Z. (2020). Types and resource potential of continental shale oil in China and its boundary with tight oil. Petroleum Exploration and Development, 47(1), 1-11. https://doi.org/10.1016/S1876-3804(20)60001-5

Zolfaghari, A., Dehghanpour, H., & Xu, M. (2017). Water sorption behaviour of gas shales: II. Pore size distribution. International Journal of Coal Geology, 179, 187-195. https://doi.org/10.1016/j.coal.2017.05.009